

<https://doi.org/10.1038/s43247-024-01553-x>

Marine heatwaves in a shifting Southern Ocean induce dynamical changes in primary production

**Manuel Fernández-Barba** , **Oleg Belyaev** , **I. Emma Huertas** & **Gabriel Navarro**

Marine heatwaves are discrete, albeit prolonged, episodes of extreme ocean temperatures that are significantly impacting marine ecosystems worldwide. However, there is limited research solely focusing on marine heatwaves and their concomitant effects on ecosystem dynamics in the Southern Ocean, known to play a major role in the Earth's climate system. Here we use daily high-resolution satellite-derived and modelled data from 1982 to 2021 to characterise general spatiotemporal patterns of marine heatwaves in the Southern Ocean, assess their physical drivers and explore their interconnections with marine biogeochemistry. We find that increasing climate change-related marine heatwave activity, primarily explained by sea-air heat fluxes and vertical diffusion anomalies, enhances net primary production through stabilization of the water column. We empirically reveal causal nonlinear relationships between ocean extremes and primary productivity, especially in the southernmost subantarctic areas where the concurrent sea ice decrease also plays a key role. Furthermore, our study shows zonally asymmetric responses of primary producers to changing physical conditions north of the Antarctic polar front. These results provide key insights into the role of marine heatwaves promoting carbon assimilation (and uptake) in the Southern Ocean through the biological carbon pump, which is crucial for constraining the oceanic carbon cycle under climate change.

During the last decades, long-term ocean warming has been shown to contribute to a rise in the Earth's surface temperature, increasing the frequency and intensity of widespread superimposed short-term extreme phenomena^{1,2}, such as heatwaves. In marine ecosystems, anomalously warm temperatures affect their structure and functioning in the form of marine heatwaves (MHWs)^{3–7}, commonly defined as discrete persistent extreme events where sea surface temperature (SST) exceeds certain criteria based on a seasonally varying climatological threshold and variability^{8–10}. Under warming conditions, the rate and degree of ecosystem change depends on the heat tolerance ranges and diversity of particular species^{11–13}. This thermal tolerance is not only dependent on the intensity of the underlying SST anomalies (SSTAs), but also on the frequency and duration of MHWs¹⁴. In this sense, impacts from MHWs not only include range shifts of marine fishes and invertebrates^{15,16} and reduction in their reproductive success and survival, but also impacts phytoplankton^{6,17}, bleaching of coral reefs¹⁸, and large-scale mass mortality outbreaks, events that are becoming increasingly common¹⁹.

When assessing impacts of MHW characteristics, it is important to clearly differentiate between the long-term externally forced warming trend from changes in internal variability. Therefore, the decision to use a fixed or moving climatological baseline to identify MHW events should be made based on the requirements of the study. While fixed baselines are more sensitive to changes in long-term mean sea temperature, they are often used when analyzing ecological impacts resulting from MHWs^{14,20}. Despite the long-term mean warming trend, which inherently increases the probability of SST exceeding a MHW threshold²¹, changes in internal system variability, resulting from a combination of both atmospheric and oceanic processes, trigger these extreme temperature episodes. For instance, atmospheric warming associated with high-pressure blocking, oceanic heating by horizontal advection, and El Niño Southern Oscillation (ENSO) events can be the main driving mechanisms^{22,23}. Consequently, MHWs have been analysed in the global open and coastal²⁴ ocean, where their globally-averaged frequency and duration have increased over time due to continued global warming^{3,4,23,25,26}. The magnitudes of ongoing

middle and low-latitudes events are expected to continue rising under anthropogenic climate change³.

In contrast, the occurrence of MHWs in higher latitudes has received limited attention²⁷. In the Antarctic region, the interaction between different processes, such as atmospheric and ocean warming (Fig. 1a), increasing precipitation²⁸ that impacts sea ice extent²⁹ (Fig. 1b), and melting of the Antarctic ice shelves³⁰ is enhancing freshwater fluxes in the Southern Ocean (SO)^{31–33}. Freshwater inputs are altering marine biogeochemical cycling in the region³⁴ and the strength and patterns of the Antarctic Circumpolar Current (ACC) system (Fig. 1a), the strongest oceanic circulation branch and a major contributor to global ocean ventilation³⁵. Similarly, anthropogenic forcing also plays a relevant role in driving climate change throughout Antarctica by increasing greenhouse gas emissions and stratospheric/tropospheric ozone changes, which intensify the polar vortex³⁶ and increase the subsurface SO heat content³⁷. Recent studies have described subantarctic phytoplankton responses due to Antarctic meltwater-driven stratification under persistent global warming^{38,39}. In the tropics and mid-latitudes, MHW-induced upper ocean stabilisation has been known to modulate decreases in chlorophyll (CHL) concentrations^{40,41}, but the impact of these extreme events over the high-latitude phytoplankton activity has not yet been addressed.

In this study, we use satellite and modelled data from 1982 to 2021 to quantify MHW occurrence throughout the SO and adjacent basins south of 40°S based on established metrics, characterising their main features and analysing their physical drivers. We further explore the consequences of the occurrence of thermal events over the SO by analysing their connections with dynamical changes in primary production. Our study provides a concise approach assessing the occurrence of MHWs in the SO, and suggest that the increasing frequency, duration and intensity of such heat events can affect circumpolar biogeochemistry, as evidenced by increased phytoplankton activity.

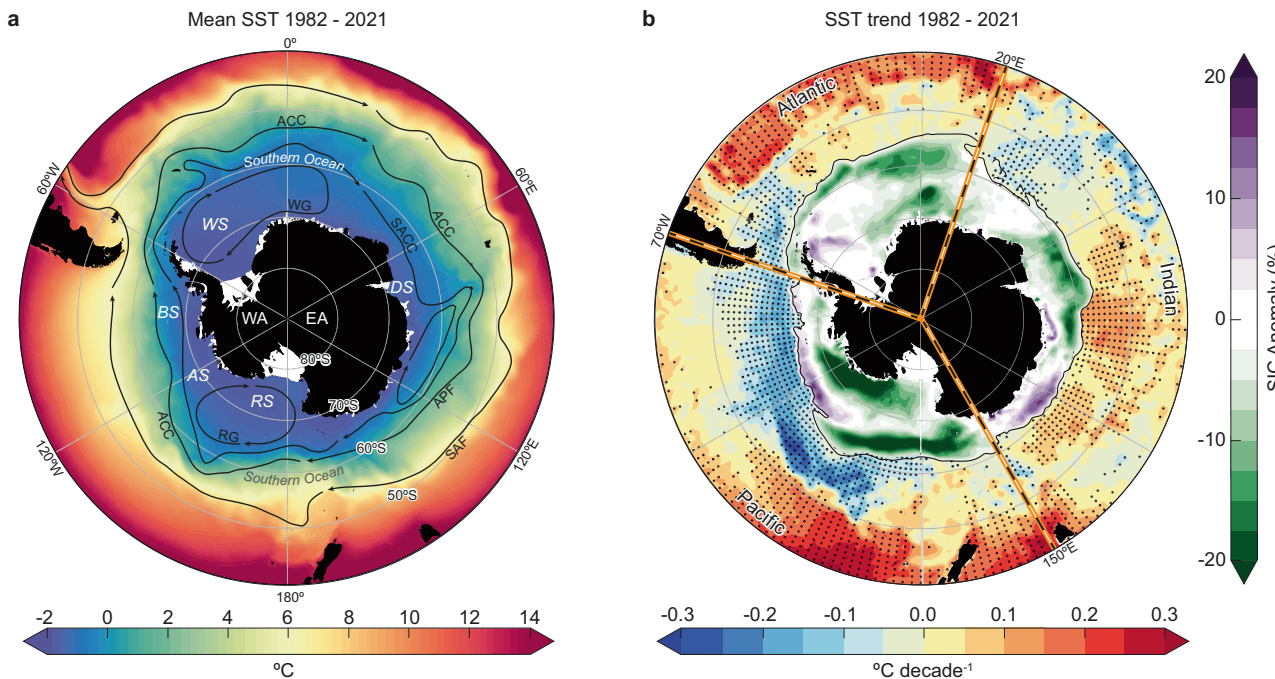


Fig. 1 | Study area: A changing Southern Ocean in the context of global warming. a Mean SST 1982 – 2021 (shading) from Climate Change Initiative (CCI) and Copernicus Climate Change Service (C3S) L4 daily reanalysis with main ocean currents and features characterised by ref. 94 in the Southern Ocean (SO) and surrounding areas (black arrows). The named features are north to south, the subantarctic front (SAF); the Antarctic polar front (APF), delimiting the Antarctic Circumpolar Current (ACC); the southern ACC (SACC); Weddell Gyre (WG), and

Results

Characterizing Southern Ocean marine heatwaves

The averages of annual MHW metrics (1982–2021), based on the conventional definition (see Methods and Supplementary Fig. S1), are shown in Fig. 2. The maximum SSTAs, which were calculated considering a reference period from 1982 to 2012, were higher at lower latitudes south of 40°S in the Pacific, Atlantic, and Indian sectors (see these divisions in Fig. 1b), and ranged from 0.6 °C to 11 °C (Fig. 2a). High maximum SSTAs were also observed in the Drake Passage (between the Bellingshausen Sea and the Scotia Sea), between the Amundsen and Ross Seas, and also across the Davis Sea and south Indian sector, ranging from 4 °C to 6 °C. All these regional maximum SSTAs were consistent with that of other MHW metrics (Fig. 2). Large-scale variations prevailed throughout the SO. This variability was associated with the patterns of the ACC System (Fig. 1a), since the ACC, enhanced by both surface and remote forcing, is the main source of net interbasin heat exchange^{32,42}. Decadal maximum SSTAs linear trends (Fig. 2b) were comparable to mean SSTAs obtained in the global ocean³ and also comparable with those in the Arctic Ocean²⁷. Furthermore, the inter-annual and multi-decadal variabilities observed south of 40°S, both circumpolarily and in sectors, in maximum SSTAs (Fig. 2c), emphasised the aforementioned patterns. Note that the annually varying area with mean Sea Ice Concentration (SIC) above 0.20 (20%) (Supplementary Fig. S2) has been masked out, since MHW metrics are less trustworthy in areas with high concentrations of sea ice and associated low SST standard deviation^{3,27,43}. However, the subantarctic region (latitudinal band between the SAF and APF, Fig. 1a) is susceptible to being impacted by sea ice melting^{29,44}. Therefore, it must be taken into consideration when explaining trends and anomalies in the subpolar SO surface signal.

The annual mean MHW frequency was 1–2 events in most of the SO (Fig. 2d), which was comparable to that in the tropical–subtropical oceans^{3,23}. The largest count per year occurred in the Davis Sea, surrounding Tasmania and New Zealand, and the southwestern Atlantic, where 2–3

Ross Gyre (RG). The main subbasins composing the SO, Davis Sea (DS); Ross Sea (RS); Amundsen Sea (AS); Bellingshausen Sea (BS); and Weddell Sea (WS).

b Decadal trends in SST (1982 – 2021) south of 40°S with Sea Ice Concentration (SIC) anomalies (2015 – 2021) from CCI C3S product. In (b), stippling indicates the linear trend is significant from zero ($p < 0.05$), and orange dashed lines separate the three large interconnected basins (Atlantic: 70°W–20°E, Indian: 20°E–150°E, Pacific: 150°E–70°W) down to 40°S.

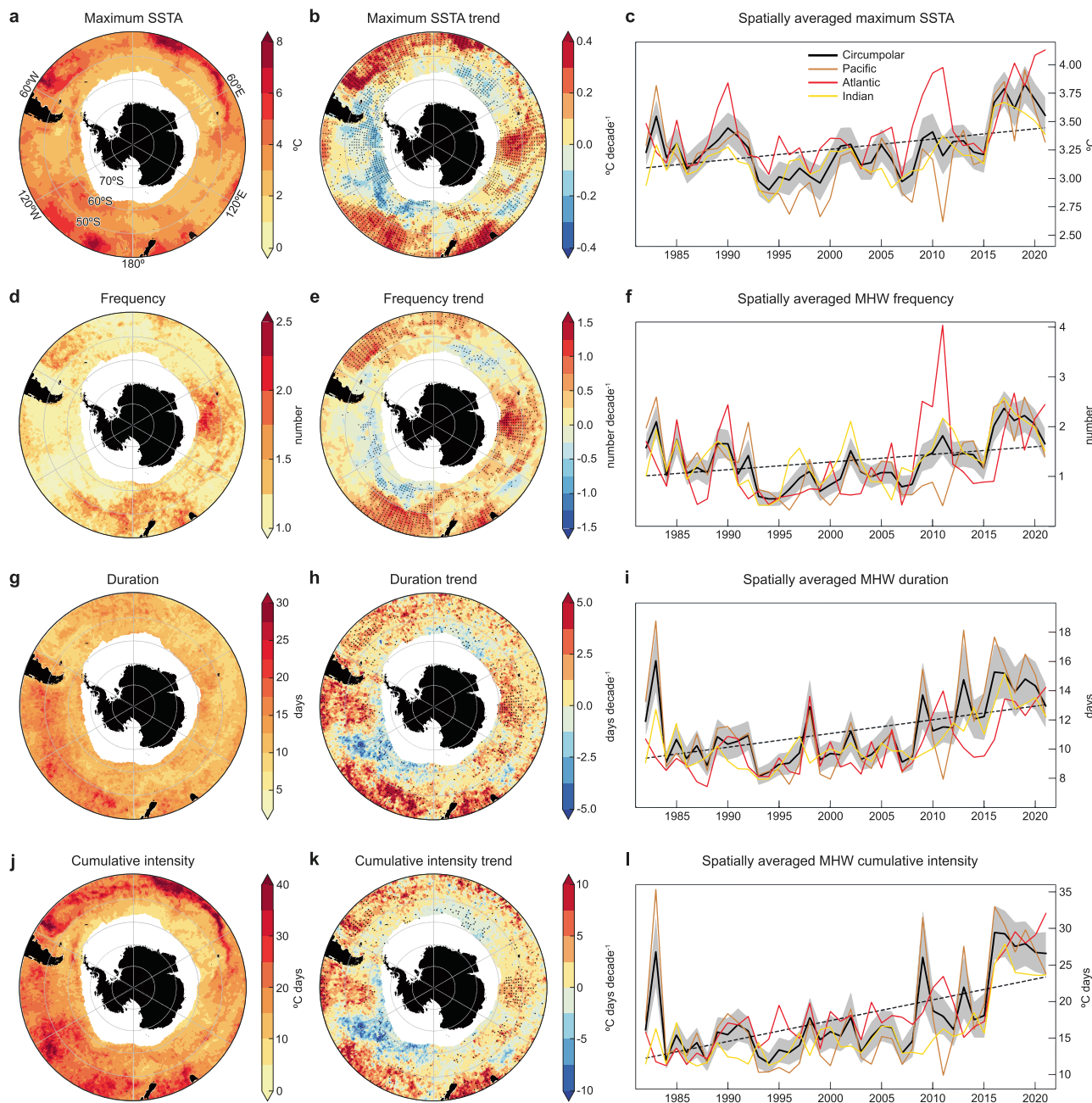


Fig. 2 | Southern Ocean marine heatwave properties. **a, d, g, j** Annual averages (1982–2021). **b, e, h, k** Linear decadal trends, and **(c, f, i, l)** spatially averaged (south of 40°S) time series of annual mean (**a–c**) maximum SSTA, (**d–f**) marine heatwave (MHW) frequency, **g–i** MHW duration, and (**j–l**) MHW cumulative intensity from CCI C3S L4 SST over 1982–2021, using the 95th percentile criterion (see methods section). In (**a, b, d, e, g, h, j, k**), the region where mean (1982–2021) SIC are greater

than 20% is masked out (Supplementary Fig. S2). In (**b, e, h, k**), the stippled areas indicate that the change is significantly different from zero at the 5% confidence level. In (**c, f, i, l**), black lines show the circumpolarly averaged time series with the linear fittings (black dotted), while brown, red and yellow lines show Pacific, Atlantic and Indian sector averages, respectively. Black shading indicates the standard error of the metrics.

discrete MHW events took place each year. Interestingly, these areas experienced increases of ~2 events per decade (Fig. 2e), indicating that MHWs are a recent phenomenon here under the global warming scenario. Similar to the situation in the global ocean³, a relationship between the spatial pattern of mean MHW frequency and duration at each grid point could be observed. Although to a lesser extent, these two MHW metrics were also negatively spatially-correlated (-0.37) in the SO and its surrounding areas. The Pacific sector was a clear long-lasting MHWs hotspot, where certain oceanic points exhibited events lasting, on average, between 20 and 30 days (Fig. 2g), which was consistent with global studies^{20,23}. The spatially averaged mean MHW duration in the Pacific region was approximately

12 days (Fig. 2i). Even though high negative duration trends were observed in the Pacific region where negative maximum SSTA trends were present (Fig. 2b), significant and positive trends were also evident in the remaining Pacific sector (Fig. 2h), as well as in the Tasman Sea and Davis Sea. On average, the Davis Sea had the highest frequency of MHW events per year, with a high positive frequency trend and, although the events were not on average the longest-lasting, their duration had significantly increased to 20 days over the past decades. This clearly identified the Davis Sea as a MHW hotspot. Because of the high magnitudes (maximum SSTA) and frequencies of their events, the northwestern Atlantic sector down to 40°S was also identified as a pronounced MHW area. To better represent the

individual MHW event strength, the cumulative intensity metric (Fig. 2j) was analysed, which combined both duration and intensity (see Methods). Therefore, on average, the degree heating days in the SO and adjacent southern basins was 17.73 °C-days per year (Fig. 2l), which, as expected, was substantially lower than that in the tropical–subtropical ocean³ but comparable to the values reported in high northern latitudes^{27,45}. Cumulative intensities of MHW were significantly higher in areas with longer and more intense MHW events (i.e., lower latitudes and ACC system). However, the significance was also high in the Davis Sea (Fig. 2k), revealing the importance of the frequency to the strength of individual events, as previously noted by ref. 46.

To better analyse the time evolution of MHWs, the annual metrics were averaged in the area south of 40°S (Fig. 2c, f, i, l) where SICs were lower than 20% (Supplementary Fig. S2). The same pattern was observed in all the circumpolarly-averaged metrics. Values declined from 1982 to 1994/1995. Subsequently, they began to increase to 2015 and then reverted towards the overall trend line. The circumpolarly-averaged maximum SSTAs were 3.19 °C during 1982–2015 and 3.7 °C during 2015–2021 (Fig. 2c and Supplementary Table S1). An increase was also evidenced in mean SSTAs (Fig. 3a), although to a lesser extent due to spatial heterogeneity around the Antarctic–SO system. Changes in SSTAs in the SO have been largely associated with changes in atmospheric pressure anomalies and near-surface wind forcing^{42,47}. In this sense, peaks in circumpolarly averaged maximum SSTA and other MHW metrics could be more evident in the Pacific time series (Fig. 2c), which appeared to be related to ENSO events, particularly linked to strong and moderate intensity El Niño events^{3,23} (1982/83, 1986/87, 1988/91, 1997/98, 2004/05, 2009/10, 2015/16 and 2019/20). As expected, ENSO seemed to be affecting the mean and variability of maximum SSTAs (Supplementary Fig. S3a–c) to a lesser extent in the Atlantic and Indian sectors, where the Tropical Southern Atlantic (TSA) and the Southern Annular Mode (SAM) indices appeared to be important^{23,48} (Supplementary Fig. S3d–i). Furthermore, an interesting decoupling between Pacific and Atlantic MHW metrics was observed, particularly in years with strong La Niña events³ (1999–2001, 2008/09, and, to a greater extent 2011/12, 2017/18 and 2021; Fig. 2c, f, i, l), which suggested a zonally asymmetric relationship between certain climate modes and MHWs in the SO.

The strengthening of MHW events in the SO can be examined in annual metrics of mean frequency, duration, cumulative intensity (Fig. 2f, i, l), total annual MHW days, and areal coverage ratio (Supplementary Fig. S4). The circumpolar average annual frequency and duration of MHWs has increased from about 1 event lasting 11 days during 1982–2015 to 2 longer discrete events of approximately 15 days during 2015–2021 (Fig. 2f, i; Supplementary Table S1). This has led to an increase in the total annual MHW days from about 16 days during 1982–2015 to 34 days during 2015–2021 (Supplementary Fig. S4a). Consistently, increases in both magnitudes (SSTAs) and durations have resulted in a considerable increase of cumulative intensity from about 16 °C-days during 1982–2015 to 28 °C-days over the last seven years (Fig. 2l). Furthermore, the ocean surface area south of 40°S subjected to at least one MHW per year has increased by approximately 20% in recent years (Supplementary Fig. S4b), with the Indian sector being the most recently frequented by an extreme event (Fig. 2e–f). However, maximum magnitudes (SSTAs) were greater in the Atlantic sector (Fig. 2a–c), while longest-lasting events occurred in the Pacific area (Fig. 2g–i). This heterogeneity highlights SO climate regionality.

When considering MHWs, it is crucial to discern not only the role of short-term but also longer-term variability. As previously noted, there was clear evidence of interannual and multi-decadal variability in the change patterns of SO MHW metrics. While zonally asymmetric SST trends (Fig. 1b) have been largely linked to climate modes and tropical–polar teleconnections^{23,31,42,47}, which are intrinsic and known as transient climate variability, the role of secular anthropogenic climate change^{36,49} should also be considered, possibly leading to the symmetric part of the (spatially-averaged) positive trends (Fig. 2c, f, i, l, and Supplementary Table S2). However, the satellite record (1982–2021) remains too short to

allow a clear discrimination between multi-decadal climate variability and human induced long-term trends.

Potential drivers of the Southern Ocean Marine Heatwaves

The variability of SST at a specific location, region, or basin can be modulated by local to large-scale climate variability²³. Local physical drivers of MHWs over the SO were assessed by examining heat term budgets available in the Modular Ocean Model (MOM4p1)⁵⁰ (Fig. 3a–i). Additionally, the correlation between MHWs and several essential climate variables from 1982 to 2021 was also explored (Fig. 3j–m and Supplementary Table S3). The annual mean heat flux anomalies in the surface ocean layer averaged during the MHW onset (i.e., build-up of heat) and decay (i.e., dissipation of heat) phases (Supplementary Fig. S1) are listed in Supplementary Fig. S5. Results from the heat budget analysis showed that temperature changes during MHWs were mainly explained by 4 most important counteracting processes (Fig. 3a–i). While ocean advection, sea-air heat fluxes, and vertical diffusion positively contributed to the formation of MHWs in the SO, as well as to the subsequent heat loss, convective vertical mixing (from the non-local part, see Methods) inherently acted in a contrasting mode. This arises from the intrinsic characteristics of this non-local term, which was incorporated in the MOM4p1 to mitigate air-sea heat fluxes when faced with negative buoyancy forcing conditions⁵⁰. During the onset phase of MHWs, the averaged circumpolar surface ocean heat gain reported in the pre-industrial control simulation was 20 W m⁻², with air-sea heat fluxes being the dominant MHW driver (Supplementary Fig. S5a). Nevertheless, in the eight-member ensemble simulation for the 1982–2021 period, the circumpolar heat gain during the onset phase amounted to 39.8 W m⁻². This was explained by the increased contribution of vertical diffusion (26 W m⁻² or 65.2%; Supplementary Fig. S5b and Fig. 3g). Despite the major role of the surface heat fluxes (Fig. 3c, d), which was especially important in the Atlantic sector, vertical diffusion emerged as the dominant process both in driving MHWs in the SO and as an overarching cooling contributor to their decline (Fig. 3g, h). This was particularly relevant across much of the areas connecting the sea ice zone (defined by averaged SIC > 20%; Supplementary Fig. S2) and the southernmost subantarctic belt along the Atlantic and Indian sectors. This finding highlighted the relevant feedback between sea ice variability and surface ocean temperature extremes in these regions (as also demonstrated in Supplementary Fig. S6a, b). Horizontal advective heat fluxes followed the ACC pathways, though they appeared to play a secondary role, affecting the development of MHWs in the SO only locally (Fig. 3a, b). However, it is important to note that the MOM4p1 model may underestimate the impact of advection, as its relatively low horizontal resolution cannot resolve mesoscale processes⁵⁰. Furthermore, the contribution of drivers did not necessarily depend on the strength of the MHWs (as measured by the cumulative intensity) in the SO (Fig. 3i), and various combinations of driving mechanisms were possible; being consistent with ref. 51 That is to say, the strongest and weakest MHW events were primarily driven by the same leading processes –positive ocean heat uptake anomalies and vertical diffusion– and were dampened by convective vertical mixing during their onset phases. While both air-sea heat fluxes and vertical diffusive processes led to the dissipation of heat, advection and contrasting vertical mixing played minor roles during the decay phases (Fig. 3i).

During the period 1982–2021, the variability in surface heat anomalies was consistent with changes in near-surface air temperature (N-SAT), and SIC over the SO (Fig. 3j–m). A significant positive correlation between monthly averaged (from November to March) SSTAs and N-SAT (Supplementary Table S3) was obtained, which indicates that the post-2015 warmer air temperature over the SO (Fig. 3j) has been reducing upward sensible heat exchange, strengthening downward infrared radiation⁵², and consequently warming the SO SST (Fig. 3l–m). The increase in the total SO sea ice extent until 2015 (Fig. 3k) led to an enhancement in reflected solar radiation over regions with substantial summer sea-ice cover⁵³, thus decreasing the absorption of solar radiation by the ocean, and resulting in cooler SST. The subsequent sudden sea ice loss resulted, on average, in warmer SSTs in adjacent subpolar areas, as previously noted by ref. 54

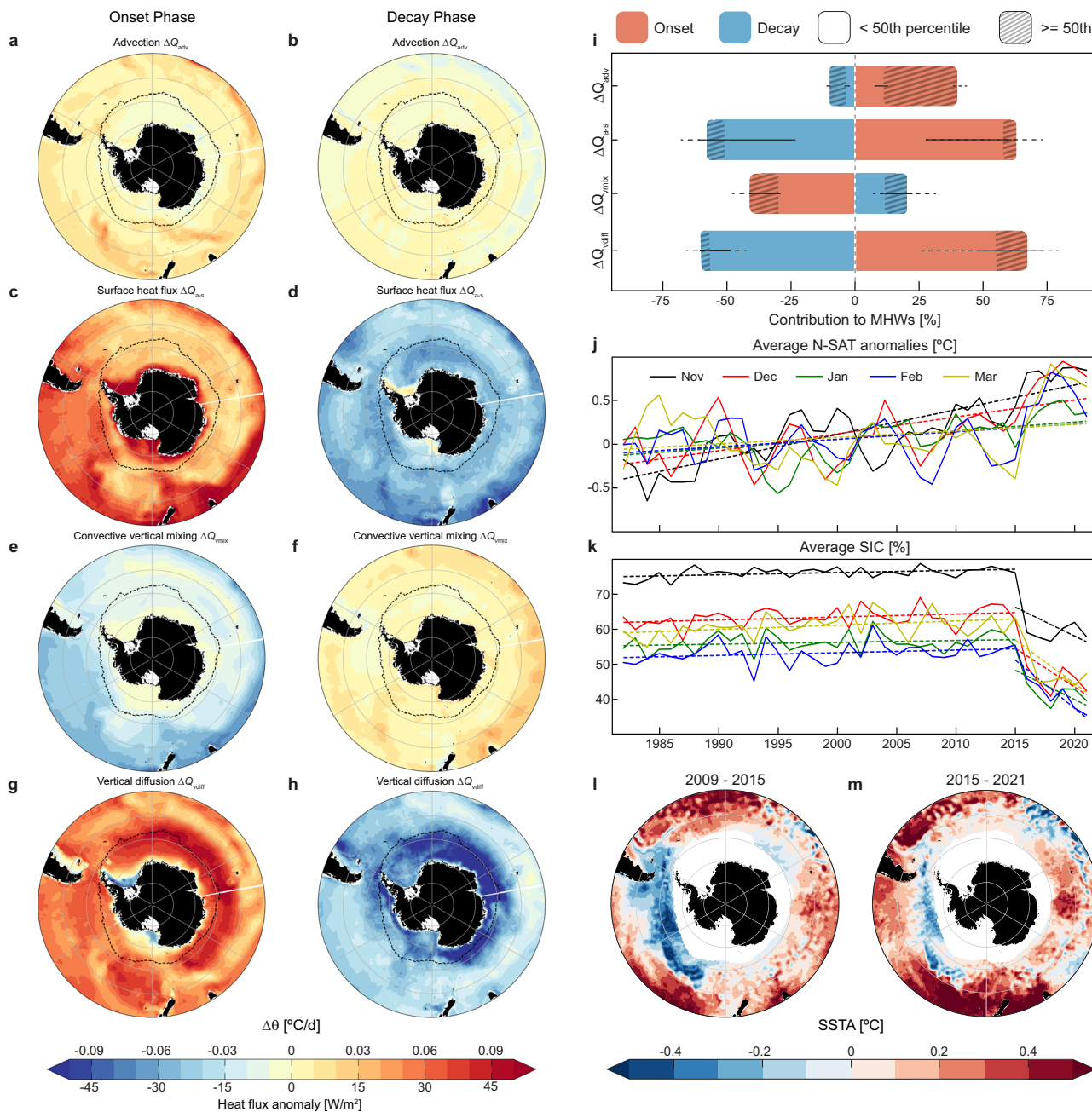


Fig. 3 | Local drivers of Southern Ocean marine heatwaves. **a–h** Simulated (GFDL ESM2M) heat flux anomalies (in W m⁻²) for the 4 most important heat budget terms during MHW (**a, c, e, g**) onset and (**b, d, f, h**) decay days over the 1982–2021 period. Black contour outlines the mean 1982–2021 SIC = 20%. **i** Circumpolar contributions (%) of these terms to the full temperature tendency during the onset (red bars) and decay (blue) phases for lower cumulative intensities of MHWs (< 50th percentile, solid bars) and for higher cumulative intensities (>= 50th percentile, hatched bars). **j–k** Annual averages of (**j**) ECMWF ERA-5 near-surface air temperature (N-SAT) anomalies (in °C) and (**k**) ESA CCI & C3S sea ice concentrations (SIC, in %) in

November (solid black), December (solid red), January (solid green), February (solid blue), and March (solid yellow). **l, m** Sea surface temperature anomalies (SSTA, in °C) from the ESA CCI & C3S SST averaged (south of 40°S where mean 2009–2021 SIC < 20%, Supplementary Fig. S2) over (**l**) seven-year period prior to the sea ice drop and (**m**) seven years later. In **i**, horizontal error bars indicate the interquartile range. A 3-year running mean filter is applied to N-SAT anomalies (**j**). In (**j–k**), dotted lines represent the linear fitting (trends are illustrated for 1982–2015 and 2015–2021 in **k**). In (**a–m**), reference period is from 1982 to 2012.

Therefore, the SIC decrease was correlated with positive SSTAs, and with the rise of MHW activities in these areas (Supplementary Table S3). During the warm months, MHWs (Fig. 2c, f, i, l) were clearly enhanced with warmer surface air temperature (Fig. 3j) and a reduction of SIC (Fig. 3k) over the SO, particularly during 2015–2021. Conversely, the weakest events occurred in years with larger sea ice cover and associated atmospheric cooling. However, N-SAT and SIC are not uniform in November–March (Fig. 3j), primarily due to the strong seasonality in the location of the high and low-pressure

centres (e.g., Amundsen Sea Low, ASL)⁵³ over the Antarctic region, which also induces spatial heterogeneity (as also seen in SSTAs in Fig. 3l, m) through alternation of offshore/onshore-winds^{53,55,56}. Despite the global warming associated to the anthropogenic impact on the Earth's climate, the sea ice extent in the SO increased until 2015⁵⁷. This has been attributed to high-latitude and tropical forcing factors^{47,57}. After 2015, the sudden sea ice loss has been driven by changes in near-surface wind stress associated with the deepening in the ASL^{47,58}. In particular, very deep depressions in ASL

result in strong offshore (southerly) winds, which in turn contribute to the formation of more sea ice over the Ross Sea through both cold atmospheric advection and offshore sea-ice drift⁴⁷. Once these sea ice masses are exposed offshore to solar heating, they result in further sea ice melt. Similarly, strong westerly winds blowing north of the Weddell Sea move sea ice toward the east⁵⁵. Conversely, onshore winds north of the Antarctic Peninsula melt and compress sea ice around the coastal zones of the Amundsen and Bellingshausen Seas⁵³ regions, where higher negative anomalies were observed (Fig. 3l, m), and therefore MHW events were least likely to occur (Fig. 2d, e).

Net primary production responses to a changing Southern Ocean

Different types of primary producers are spread across diverse regions of the SO, with those inhabiting the surface layers (i.e., ice-edge and mixed-layer phytoplankton) being observable (or derivable) via remote sensing⁵⁹. In the southernmost latitudinal band of the subantarctic region, sea-ice melting is one of the greatest sources of trace elements, such as iron (Fe), to the Antarctic waters⁶⁰, fertilizing large high nutrient-low chlorophyll areas and promoting ice-edge phytoplankton growth^{38,61,62}. The sudden drop in SIC, experienced from 2015 (Fig. 3e), suggests a possible shift in inputs of micronutrients, therefore affecting these primary producers. With the general increase in MHW occurrence throughout the southernmost subpolar SO, higher SSTAs would induce an increasingly shallower mixing layer²⁰, contributing to the accumulation of nutrients and trace elements from sea-ice melting near the surface^{38,63}. A significant inflection point can be evidenced in modelled Fe concentration trends from 2015, with an overall reduction in seawater Fe quantity surrounding the Antarctic continent (Supplementary Figs. S7a–c). These negative trends can be attributed to the presence of larger amounts of Fe being released from anomalously rapid sea-ice melting, thereby triggering higher rates of Fe uptake⁶⁴ and consequently phytoplankton proliferation. Similar to modelled Fe, major modelled nutrients in these areas also experienced remarkable inversion in concentration trends, likely reflecting consumption by the phytoplankton biomass (Supplementary Fig. S7d–l).

In this sense, the Carbon-based Production Model (CbPM) outputs were consistent with the modelled nutrient depletion trends in the SO, where a notable increase in ice-edge marine productivity was observed in the years following the post-2015 SIC drop and concurrent highest MHW activity along subantarctic regions (Fig. 4a). Two clear peaks in net primary production (NPP) in 2004/05 and 2011/12 –especially in the Atlantic sector– were also observed coinciding with strong MHWs (Fig. 2c, f, i, l) during these El Niño and La Niña years³, respectively. Distinctive distributions of NPP were observed when rates were averaged over the months (from November to March) under MHW conditions, and over months without MHWs from 1998 to 2021 (Fig. 4b). The average NPP rates manifested an elevation during MHWs, with a difference of approximately 100 mgC m⁻² day⁻¹ compared to the NPP in the same months where the SST remained within its climatological standards. Additionally, the average minimum NPP increased from 1 to 74 mgC m⁻² day⁻¹ under MHW influence. These results were consistent with the relatively lower SIC (greater density at lower values) and shallower mixed-layer depths (MLD) during the MHW conditions (Fig. 4c, d). Such conditions are conducive to retaining meltwater-induced nutrients and trace elements within the euphotic layer, thus promoting phytoplankton proliferation³⁸. Furthermore, causal analysis through convergent cross mapping (CCM)⁶⁵ highlighted the intricate interdependencies within the complex SO system (Fig. 4e–g). The predictive skill for NPP based on the time series of Max SSTA (NPP xmap Max SSTA; Fig. 4e) exhibited spatial heterogeneity, with high cross-map skills in subantarctic regions and the weakest skills obtained in the most dynamic areas (between ACC and the subantarctic front). However, the generally moderate skill of cross map estimates suggested that extremes of temperature alone were not the sole determinant of primary production variability. Additionally, the influence of sea ice melting on NPP could be appreciated in the southernmost subantarctic band

(Fig. 4f), where moderate causal linkages emphasised the important role of ice dynamics within these areas. Nonetheless, the variable that best identified the state of NPP was the MLD, with the highest and generally homogeneous values of cross-map skills (Fig. 4g). This underscored the critical role of shallower MLDs in concentrating light and nutrients in the upper layers of the SO, facilitating the thriving of phytoplankton⁵⁹. It is imperative to highlight that these 3 physical variables (Max SSTA, SIC, and MLD) were closely interlinked, with a significantly higher forcing impact of Max SSTA on SIC and a close causal bidirectional relationship between MLD and temperature extremes (Supplementary Fig. S6), as previously demonstrated by ref. 20.

Thus, causation is transitive (eg., if Max SSTA leads to shallower MLD –and vice versa–, and shallower MLD enhances NPP in the SO, then Max SSTA and NPP are also indirectly causally linked). Conversely, prediction skills of the reconstructions of Max SSTA, SIC, or MLD from the true values of NPP, as expected, were lower (Supplementary Fig. S8). Therefore, despite the bidirectionality in the system, results from the empirical dynamic modelling (EDM) showed the measurable non-linear causal coupling between the changing upper-layer physical conditions of the SO and the spatiotemporal dynamics of the primary producer communities (Fig. 4e–g).

Furthermore, two regionally focused case studies were conducted to illustrate how sustained high air (N-SAT) and sea (MHW) temperatures, along with associated low SIC and a shallower MLD, led to the occurrence of high net primary production (HNPP) events in subantarctic regions (Fig. 5), through the simultaneous stabilisation of the water column and the increased inputs of micronutrients to the surface ocean. In order to uphold a conservative approach, consistent with the methodology applied to characterise the MHW events, the HNPP events indicated episodes where primary production surpassed the 95th percentile of its seasonal cycle. In the case of the Davis Sea, where sea ice has diminished over time, the first highlighted MHW event occurring in the early summer of 2016/17, led to an increase in primary production, following the melting of sea ice and the shallowing of the MLD (Fig. 5a). In the case of the subpolar region encompassing the Amundsen and Bellingshausen Sea (Fig. 5b), after a rapid decline in SIC in late 2016, its coverage rebounded by late 2017. This area exhibited negative trends in the surface temperature signal and, therefore, negative MHW trends. The increase in air temperature and sustained ocean changes (as demonstrated by ref. 66 and also presumably reflected in the variability of the SST signal) resulted in pronounced sea ice retreat by late 2016. This was accompanied by extreme temperatures, along with HNPP episodes in this area, extending until May 2017. Later in winter, the development of sea ice and a marked decrease in both surface air and sea temperatures co-occurred with standard primary production rates (compared to its seasonal cycle) in this area (Fig. 5b). Nevertheless, it was evident that in both cases, the seasonal minimum of N-SAT and SST aligned with peak concentrations of SIC. As temperature rises during austral summer, so does primary production. Furthermore, it was also evident that under extreme temperature events (MHWs), HNPP events occurred (Fig. 5a, b).

It should be pointed out, however, that predicting a single response of phytoplankton to extreme temperature conditions in the SO is challenging. There are many different phytoplankton groups in the Antarctic waters, each responding differently to environmental changes^{17,59,67}. Additionally, due to its vast expanse, ocean physics is not uniform everywhere in the SO (as seen in Figs. 1–3). Therefore, an interesting asymmetry was observed not only meridionally but also zonally in the response of primary producers to temperature extremes (Fig. 4a, e). As previously suggested by ref. 48, this zonal asymmetry around the higher subantarctic region was closely linked to the variability of the limiting factors for phytoplankton growth in each area, where both sea-ice melting and ocean surface warming played a critical role in stabilising and transporting micronutrients to the surface layer. Nevertheless, our assessment also showed that the relative importance of temperature extremes as a limiting factor for phytoplankton growth may be

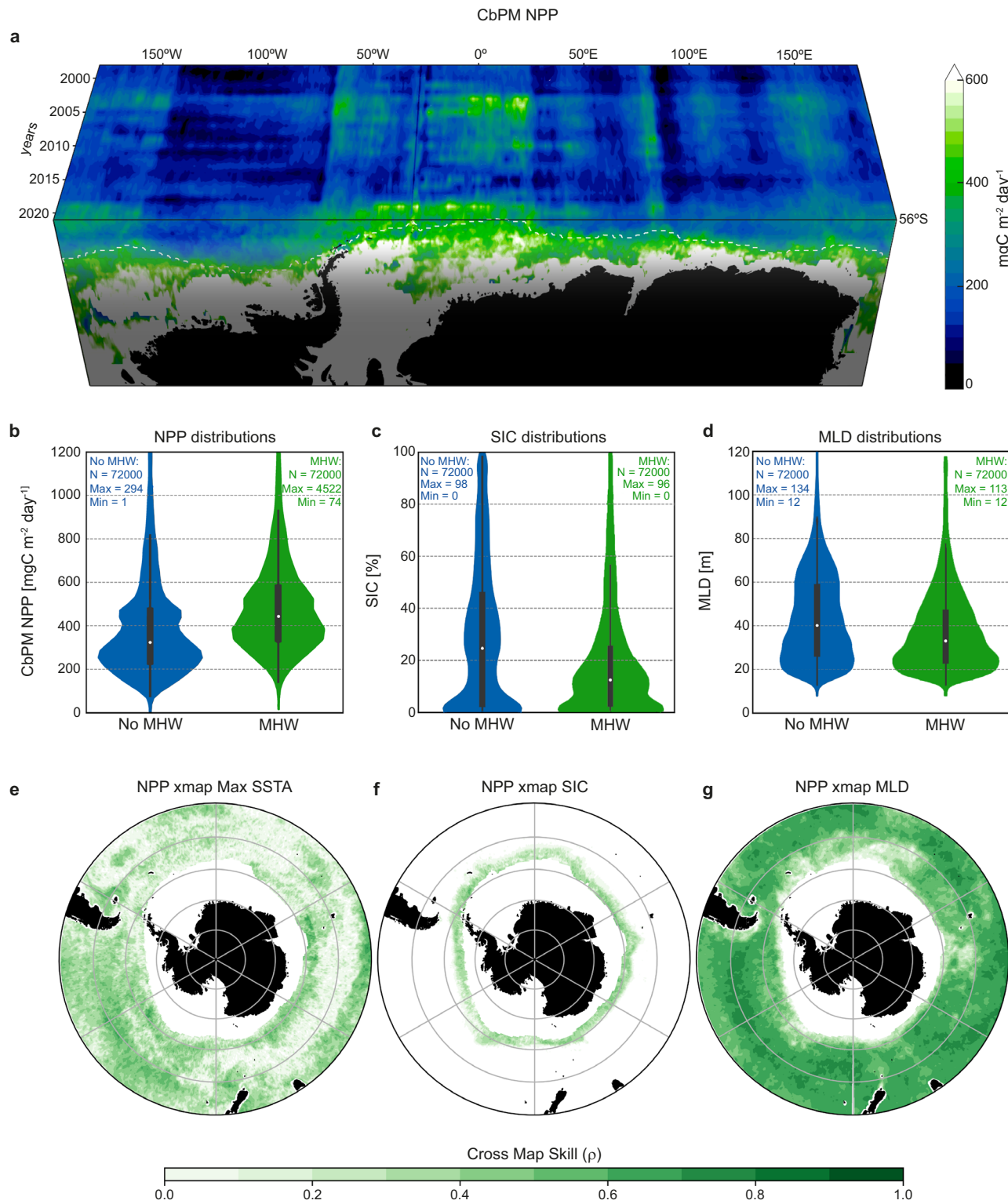


Fig. 4 | Net primary production (NPP) responses to a changing Southern Ocean. (a) Monthly averages (1998–2021) of NPP from the carbon-based production model (CbPM) north of the subantarctic band marked by the contour of 20% annual mean (1982–2021) SIC (white dashed line). b–d Violin plots displaying the distributions of (b) NPP, (c) SIC, and (d) mixed-layer depth (MLD) under MHW (green) and without MHW (blue) conditions from November to March (1998–2021). e–g Causal interactions through Convergent Cross Mapping

(CCM)⁶⁵ of the impacts of monthly (e) Max SSTA, (f) SIC, and (g) MLD, on the NPP from 1998 to 2021 south of 40°S where SIC < 20% (Supplementary Fig. S2). Skills of cross-map estimates are indicated by the correlation coefficient (ρ). In (a), time (months) is represented in the z-axis of the 3D Hovmöller diagram, with December 2021 shown on the front face as reference. Note that the NPP values within the sea ice zone, such as those shown for December 2021, are not included in the calculation of averages.

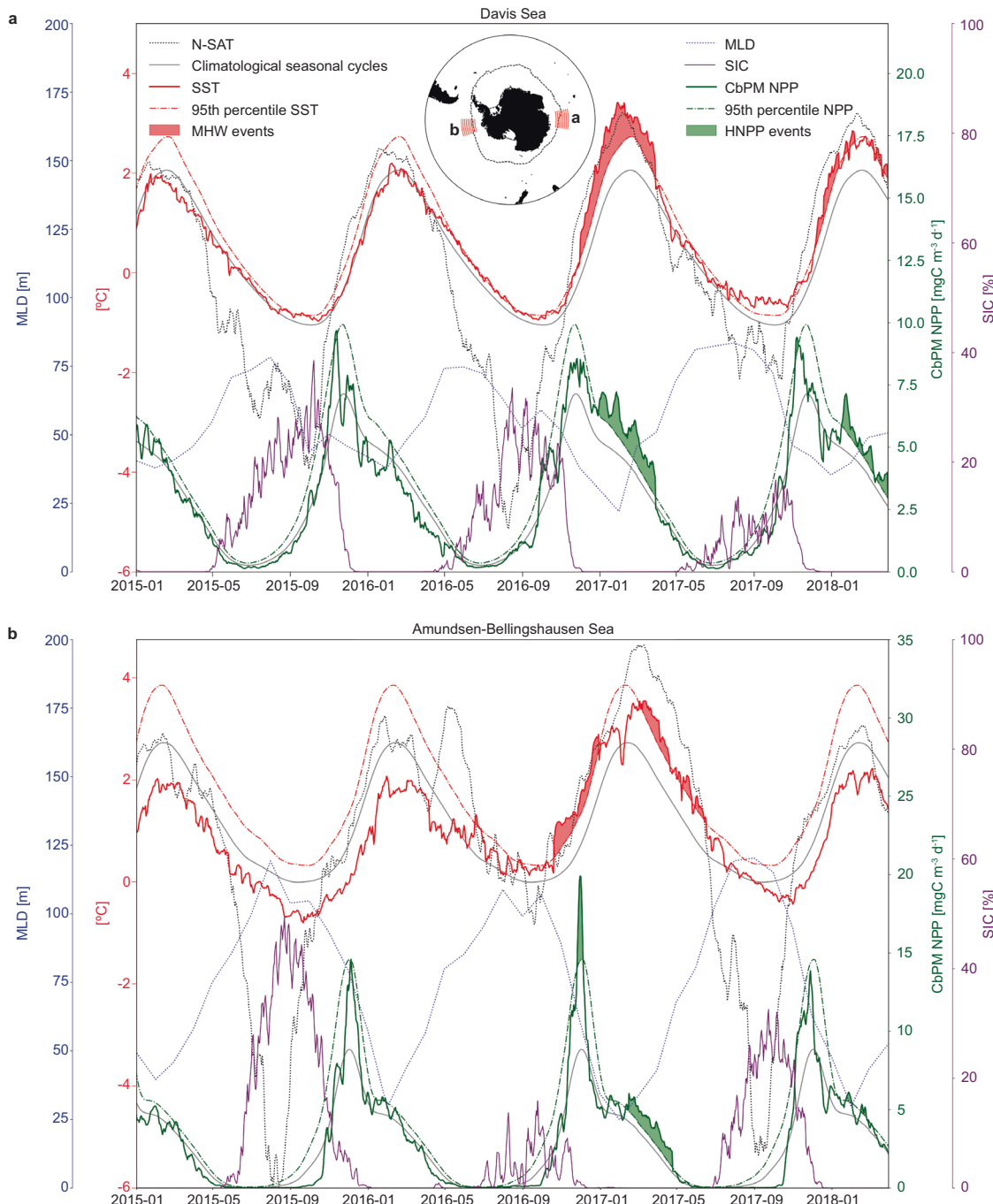


Fig. 5 | Compound MHW and HNPP events in the Southern Ocean. **a, b** 2015-01 to 2018-03 time series of ECMWF ERA5 near-surface air temperature (N-SAT, black dotted), GLORYS12V1 MLD (monthly; dark blue dotted), CCI&C3S SST (red solid) and SIC (purple solid), and CbPM Net Primary Production (NPP, green solid) rates averaged for the Davis Sea (**a**) and for the Amundsen-Bellingshausen Sea (**b**) areas.

These regions are depicted in the map in (**a**). A MHW occurs (red shaded area) when the SST (solid red line) exceeds its 95th percentile (dashed red line). A HNPP event (green shaded area) occurs when the NPP (solid green line) is above its 95th percentile (dashed green line). Compound MHW and HNPP events occur when MHW and HNPP co-occur. In (**a, b**), a 7-day running mean filter is applied to N-SAT.

reduced in highly dynamic areas, such as the ACC pathways (between outer subantarctic and higher subtropical SO; Fig. 4e). Other factors, driven by the vigorous dynamics of the ACC, such as vertical mixing (Fig. 4g) and nutrient availability (Supplementary Fig. S7), could be playing a more critical role in these regions, where the phytoplankton composition (i.e., size classes) is also very different from that in the colder, higher-latitude waters of the SO^{59,68}. Moreover, it is also necessary to consider that extreme temperatures affect grazer communities, such as Antarctic krill (*Euphausia superba*), which control phytoplankton biomass⁶⁸, ultimately modulating their regional responses.

Discussion

This study provides key insights into the close relationship between MHW events and phytoplankton productivity in the SO, which was previously suggested⁴⁰, albeit overlooked by existing literature^{3,23–26,46}. As in the global open ocean and coastal areas^{3,23,24,46}, the SO experienced MHWs of comparable magnitudes (Fig. 2a, d, g, j) to those occurring in tropical and subtropical latitudes. Furthermore, the regionally-averaged frequency, duration and intensity of these extreme heat episodes increased over the years (Fig. 2b, c, e, f, h, i, k, l) under persistent global warming²⁶. Besides the long-term warming temperature trend, which in turn increases the

probability of SST exceeding a MHW threshold^{21,69}, there were many physical mechanisms that modulate these anomalously warm marine events^{3,20,22,23}. During the austral summer, warmer surface air temperatures (Fig. 3c, j), associated changes in near-surface wind stress (closely linked to the deepening in the ASL)^{47,58}, and a related reduction in SIC (Fig. 3g, k) seemed to be the main drivers causing Antarctic waters to warm above the climatological baseline (Fig. 3l–m). Therefore, SO MHWs clearly intensified after the sudden post-2015 sea ice loss, when upward sensible heat exchange was reduced and downward infrared radiation was strengthened, as reported in the results from heat flux analysis (Fig. 3 and Supplementary Fig. S5). In contrast, less intense MHW activities were observed during years when SO sea ice and the reflected solar radiation increased. An intensification in MHWs during strong and moderate ENSO years^{3,23} was also detected, especially in the Pacific sector (Supplementary Fig. S3a), where the alternation of El Niño/La Niña events appeared to modulate to some extent the average variability of SST. Moreover, the prevalence of persistent atmospheric patterns over the Pacific sector, such as ENSO, could sustain anomalies over longer periods²³ (Fig. 2g). In the Atlantic and Indian sectors, surface dynamics played an important role in amplifying thermal anomalies, as presumably observed in Fig. 2a, j and as evidenced in the heat budgets analysis (Fig. 3 and Supplementary Fig. S5). Furthermore, in these regions, TSA and SAM appeared to be the dominant climate modes of variability²³ (Supplementary Fig. S3d–i). This also highlighted the importance of remote forcing on surface temperature variability, which affected regional scales asymmetrically in the SO. Nevertheless, when analysing MHWs, it is also important to consider the role of secular (anthropogenic) climate change³, which could be responsible for the symmetric part of the positive trends in SO MHWs (Fig. 2c, f, i, l). Unfortunately, the satellite record was not long enough to clearly discriminate between multi-decadal climate variability and long-term trends.

Results presented in this study indicated a tight linkage between the increase of MHWs and stimulated biological activity in the SO (Figs. 4, 5). The impacts of MHW-induced mixed-layer shoaling on phytoplankton have been studied in the global ocean^{5,22,40}, where weaker phytoplankton blooms are suggested to be occurring in the tropics and mid-latitudes as a consequence of ocean stratification and associated surface nitrate depletion⁴¹. Moreover, global marine ecosystems are increasingly vulnerable to MHWs under the projected increase in frequency, duration, and intensity of these events⁴. However, little attention has been paid to the effect of these extreme events on high latitude ecosystems^{40,70,71}, even though recent studies suggest that climate change will alter the distribution of basin-scale NPP across open waters and sea ice regions in the SO^{59,63}. In contrast to the situation in the temperate and tropical zones, in high-latitude nutrient-enriched regions and with generally deep mixed layers, MHW-driven stratification increases the residence time of phytoplankton in the euphotic layer, allowing a greater exposure of primary producers to light⁴⁰. Additionally, in the southernmost subantarctic latitudinal band, a shoaled depth of mixing, along with increased inputs of the most limiting micronutrient in the SO, i.e., iron, from SO sea-ice meltwater^{38,72}, would trigger photosynthesis (Fig. 4; Supplementary Figs. S7c and S4o). Therefore, our analysis empirically revealed causal relationships between MHW occurrence in the subantarctic SO (and southern adjacent basins) and an enhanced biological activity by phytoplankton (Fig. 4e). Our results also showed a rapid post-2015 SIC decrease and concurrent sustained and elevated N-SAT as a driver promoting compound (physical and biogeochemical) changes in the southernmost subantarctic regions (Fig. 5) through ocean stratification and surface nutrient inputs (Supplementary Fig. S7). Specifically, compound MHW and HNPP events were primarily observed in late summer, a few months after the seasonal minima of MLD and SIC were reached (Fig. 5). These results were in agreement with the overall trend reported in the subantarctic SO of increasingly shorter-duration phytoplankton blooms that initiate later as a consequence of climate change³⁹. These

alterations in the phenology of phytoplankton are critical, as they may lead to a temporal mismatch between the peak abundance of phytoplankton and the peak demand for these resources by grazers in the food chain⁷, which could have cascading effects on the subantarctic marine ecosystem. However, phytoplankton responses to changing climate have been shown to be zonally asymmetric in the SO^{48,59,68}. Although these organisms may respond differently under discrete and extreme warming events, our results also showed zonal heterogeneity in the NPP dynamical responses to changing physical conditions in the SO (Fig. 4e–g). It should be highlighted that MHWs alone are not the sole direct cause of increased NPP in the vast SO. In fact, MLD, which also led to temperature extremes (Supplementary Fig. S6c), played a major role in the overall enhanced NPP activity south of 40°S (Fig. 4g). Many processes can be involved in the dynamic response of the extensive SO phytoplankton communities to a changing climate. Among them, species-specific responses to environmental stress, competition for resources, and trophic interactions (e.g., grazing)⁶⁸ would explain a considerable part of the NPP response in the SO. Furthermore, dominant limiting factors (i.e., light availability and concentration of nutrients in sea-water), impacted by changes in SO sea ice concentrations and MHWs-induced mixed layer shoaling, would likely be affecting the growth rates of phytoplankton communities from local to regional scales along the subantarctic region (Fig. 5). These factors may also condition the composition of phytoplankton functional types (PFTs). In fact, phytoplankton diversity increases in the SO under persistent global warming^{63,73}. All these considerations must be taken into account when evaluating dynamic changes in phytoplankton communities in the SO. Nevertheless, the massive variety of phytoplankton species and their differing response to environmental changes makes it challenging to predict a global and single phytoplankton response to extreme events. Future analyses based on SO MHW-induced plankton phenology changes would be required to properly assess the impacts of these extreme events over particular PFTs. Dynamic shifts in phytoplankton could have the potential to modulate carbon (C) uptake, fixation, and export in the SO^{38,48,63} which, in turn, modulate the global climate³⁵. Therefore, although additional studies are needed to understand long-term interactions between MHWs and CO₂ fluxes in the SO to forecast the dynamics of the ocean C cycle under climate change, this study provides evidence indicating that short-term warm extremes (i.e., MHWs) could have the potential to modulate C absorption in the SO due to the effect on the biological carbon pump.

Methods

ESA CCI & C3S sea surface temperature and sea ice concentration

The European Space Agency (ESA) SST Climate Change Initiative (CCI) and Copernicus Climate Change Service (C3S) reprocessed analysis (Level 4) is a daily SST product over the global ocean with 0.05° x 0.05° horizontal grid resolution from 1981 to 2021^{74,75}. The CCI SST provides daily average SST at 0.2 m depth, which is close to the nominal depth of drifting buoy measurements, using series from the (advanced) along-track scanning radiometer ((A)ATSR), sea and land surface temperature radiometer (SLSTR) and AVHRR. The biases in satellite observations were adjusted by recalibrating radiances using a reference channel, thus giving a stable product. CCI applies a variational assimilation scheme to generate a gap-filled estimate of daily-averaged SST. CCI (1981–2016) and C3S (2017–onwards) product is available at Copernicus Marine Service (CMS) (<https://doi.org/10.48670/moi-00169>, last access: November 2023). We then extracted SST and Sea Ice Concentration (SIC) data from the Antarctica-centered sub-region down to 40°S. We also re-gridded the CCI & C3S data in 0.05° resolution using simple arithmetic averaging, thus obtaining a 0.5° resolution product, for comparison purposes.

ECMWF ERA5 near-surface air temperature

The state-of-the-art European Centre for Medium-Range Weather Forecasts (ECMWF) ERA5 reanalysis⁷⁶ (<https://www.ecmwf.int/en/forecasts/dataset/ecmwf-reanalysis-v5>, last access: November 2023), replacing the ERA-Interim reanalysis with enhanced features, is an Integrated Forecasting System (IFS)-based product within C3S that provides an hourly-detailed record of global weather and climate variables at half the horizontal resolution from 1950 onwards. This reanalysis uses a four-dimensional variational assimilation system and has been widely validated around Antarctica, showing the best throughput with respect to other reanalysis products^{77–79}. We retrieved hourly 2-metre temperature (T2m) data with a horizontal resolution of 0.5°. We then averaged hourly values of each day to obtain annual means.

GLORYS12V1 mixed layer depth

The CMS Global Ocean Reanalysis and Simulations 12v1 (GLORYS12V1) provides daily to monthly mean files of physical variables from the surface to the bottom across the global ocean. The outputs, including temperature, salinity, currents, MLD, etc.; are displayed with a horizontal resolution of 1/12 (0.083°x0.083°) degree, effectively resolving global ocean eddies. GLORYS uses the Nucleus for European Modeling of the Ocean (NEMO) as its core ocean model, which is driven by surface conditions provided by the ECMWF. Initially, it used ERA-Interim data, shifting to ERA5 data in recent years. This model integrates data from satellite altimetry, SST, sea ice coverage, as well as temperature and salinity profiles from the in-depth and quality-assured Coriolis Ocean database ReAnalysis (CORA) provided by CMS. This integration helps refine forecasts by addressing errors at smaller scales. Additionally, the employment of a 3D-variational scheme allows for adjustments to the large-scale, slowly-evolving biases (<https://doi.org/10.48670/moi-00021>, last access: March 2024). We retrieved daily MLD files from 1998 to 2021. We then re-gridded them to 0.5° grid locations, and calculated the maximum monthly MLD values.

Global ocean biogeochemistry hindcast

The Mercator-Ocean global ocean biogeochemical L4 product provides daily to monthly 3D hindsight for biogeochemical fields from 1993 to 2020 at 0.25°x 0.25° and on 75 elevation levels. It uses the latest NEMO version with PISCES biogeochemical model to output, although with no assimilation scheme, automatic and human quality control-passed data. Monthly means of surface (upper 30 m) chlorophyll and nutrient (iron, nitrate, silicate, phosphate) concentrations are freely available at <https://doi.org/10.48670/moi-00019> (last access: November 2023). We re-gridded data to half the horizontal resolution.

CbPM net primary production

In order to estimate MHW-associated changes in phytoplankton carbon biomass in the SO, we applied the updated Carbon-based Production Model (CbPM)⁸⁰, which was described by ref. 81. and first applied in the SO by ref. 67. This model allows the biomass estimation from particulate back-scattering (bpp) and phytoplankton absorption (chlorophyll-to-carbon ratio) coefficients from three complementary sensors (MODIS, SeaWiFS and VIIRS). The updated CbPM NPP calculation is described as the product of carbon biomass, growth rate, and a function of depth-dependent photoacclimation and vertical variations in nutrient stress (i.e., nitrocline depth). It must be emphasised that there are uncertainties associated with the NPP rates derived from the CbPM. There are various models that derive NPP from satellite data, and each provides different estimates in the SO⁸². Nevertheless, in our study, the CbPM was chosen over alternatives, like the Vertically Generalized Production Model (VgPM), due to its superior capability to directly relate satellite-derived chlorophyll observations to carbon-based productivity. The CbPM is specifically calibrated for carbon flux estimation, making it more suitable for studies focused on carbon dynamics in marine environments^{80,81}. This was crucial in our study region (SO), where carbon uptake plays a key role in the global carbon cycle⁶³. We retrieved 1080 by 2160 monthly (1998–2021) CbPM NPP product

from http://orca.science.oregonstate.edu/npp_products.php (last access: November 2023), and suitably re-gridded into 0.5°.

Defining and monitoring marine heatwaves in the Southern Ocean

The detection of MHWs from daily CCI & C3S SST data was based on the satisfaction of the following three criteria: (a) SSTAs should be higher than the seasonally varying 95th percentile (threshold), based on the 1982–2012 period, (b) the high SSTAs should be prolonged for at least five consecutive days with gaps of less than three days and (c) average SSTs should be warmer than long-term mean summer temperature (LMST)^{27,83}. The Python code followed to identify MHWs is freely available in <https://github.com/ecjoliver/marineHeatWaves>.

The fixed climatological SST mean was calculated from the daily SST data from 1 January 1982 to 31 December 2012 (31 years), following the formula (Eq. (1)):

$$T_m(j) = \sum_{y=y_s}^{y_e} \sum_{d=j-5}^{j+5} \frac{T(y, d)}{11(y_e - y_s + 1)} \quad (1)$$

where T_m is the climatological SST (in °C) averaged over the period mentioned above, to which all values are relative; j is the day of the year; y_s and y_e are the start and the end of the climatological base period respectively; and T is the daily SST on the day d of a year y . Then, daily SST percentiles (95th percentile threshold, $T_{95}(j)$) (Eq. (2)) were calculated for each calendar day (e.g., January 15), based on climatological SST mean (X), using a centered 11-day data window (e.g., January 10–20) within the climatology period and smoothed by applying a 31-day moving average, following Hobday et al.

$$T_{95}(j) = P_{95}(X) \quad (2)$$

The use of the 95th percentile instead of the 90th percentile is meant to rule out the MHWs due to the uncertainty of ice-SST statistics, as described by ref. 27. In order to test the sensitivity of the MHW detection to the threshold, the authors compared MHWs in percentile thresholds of the 97.5th, 95th, and 90th criteria in the Arctic region. Results showed that changes in thresholds, although affecting the detection of individual MHWs, have a slight overall impact. Furthermore, areas with high concentration of sea ice (i.e., oceanic grid points with averaged annual sea ice concentrations exceeding 20%, following refs. 29,44) have been masked out to prevent misleading effect³.

The use of LMST criterion (c) is due to the tolerance of polar marine species on SSTs lower than LMST⁸³. Applying LMST allows us to eliminate MHWs in wintertime when SSTs satisfy the criteria (a) and (b), but the SST is lower than LMST. LMST was calculated (Eq. (3)) over each oceanic grid point (location) by identifying the day of the year (e.g., February 15) when daily SST climatology was at maximum and then calculating the 91-day average SST centered on this date (from January 1 to April 1, considering 28 days in February).

$$LMST = \sum_{d=j-45}^{j+45} \frac{T(d)}{(d_e - d_s + 1)} \quad (3)$$

where, d_s and d_e are the starting and the ending days of the maximum SST-centered period, respectively. For the calculation of LMST, $T(d)$ is the maximum daily SST climatology.

For instance, according to the above MHW definitions, strong MHWs are detected in the Scotia Sea (Atlantic sector of the Southern Ocean) from the end of January to the end of March 2020, as observed in the SSTs surrounding South Shetland Island (61°S 60°W; Supplementary Fig. S9a) or in the Drake Passage (58°S 61°W; Supplementary Fig. S9b) which exceeded the 95th percentile threshold and LMST. Moreover, prolonged MHW events over the Davis Sea (60°S 88°E; Supplementary Fig. S9c) and Ross Sea (63°S

178°E; Supplementary Fig. S9d), can be detected, where SSTAs are higher than the threshold and LMST for approximately three months.

Annual marine heatwave metrics

Measuring the overall strength of MHWs, as well as their impact on marine species, is becoming increasingly important. To describe these physical phenomena, most of the annual indices applied in previous studies were used here.

As discrete events, MHWs occur over a time period in which temperature exceeds the defined threshold. When a MHW is detected, its mid-time is calculated by averaging the start and end times. MHW duration is the time interval (days) between the start and end dates. Since there may be multiple events in a given year, the mean duration can be defined by averaging the durations of all events in that year. The total duration can also be defined by summing periods of all events.

MHW frequency is the total number of events (i.e., annual MHW event count) within a year. In contrast to the situation in the tropical oceans, a MHW cannot last from one year to the next in Arctic latitudes. This is associated with the seasonal variability of SST. Nevertheless, the austral warm season lasts from December to March, thus an event can occur within two different years in high Southern latitudes. When this occurs, the event is counted in the year in which it begins.

The mean SSTAs and maximum SSTAs of all MHW events quantified within a year are used to calculate the mean and maximum magnitude for the given year, respectively. The overall strength of MHWs should be evaluated in conjunction with the magnitude and other annual metrics, such as the previously-mentioned duration, frequency, or the total area coverage of MHWs. For example, when assessing MHW-associated risks in the environment, it is very important to study the cumulative intensity^{20,46}, which takes into account not only the underlying SSTAs but also its integration over the duration of an event (i.e., the degree heating days).

To study the spatial extent of MHWs, the areal coverage was calculated as the ratio between the oceanic domain with MHWs in a year and the total ocean area south of 40°S.

Climate Index metrics

In our analysis of MHW activities in the SO, we considered a close relationship between these extreme events and, particularly, three climate metrics that are linked with influential modes of variability in the climate system. These three climate mode indices are described below.

Oceanic Niño Index (ONI) – The three-month running mean of NOAA ERSST.V5 sea surface temperature (SST) anomalies is calculated for the Niño 3.4 region (5°N–5°S, 120°–170°W). This calculation is based on a changing base period consisting of multiple centered 30-year base periods. The anomalies for successive 5-year periods in the historical record are derived by using these 30-year base periods (source: www.cpc.ncep.noaa.gov/products/analysis_monitoring/ensostuff/ONI_v5.php, last access: November 2023).

Tropical Southern Atlantic (TSA) Index – Averaged anomaly of the monthly HadISST and NOAA OI SST from Eq-20°S and 10°E–30°W, following⁸⁴ (source: <https://psl.noaa.gov/data/correlation/tsa.data>, last access: November 2023).

SAM Index – An observation-based index that quantifies the intensity of the Southern Annular Mode and is calculated by the surface pressure difference between 40°S and 65°S (source: www.antarctica.ac.uk/met/gjma/sam.html, last access: November 2023).

Analysis of local drivers of marine heatwaves in the Southern Ocean

To assess the local physical drivers of MHWs, we made use of a global, fully coupled carbon-climate Earth System Model (ESM) developed at the National Oceanic and Atmospheric Administration's (NOAA) Geophysical Fluid Dynamics Laboratory (GFDL)⁸⁵. The GFDL ESM2M couples an oceanic circulation model (MOM4p1) to an atmospheric circulation model (AM2), and incorporates a land model (LM3.0), representations of sea ice

and iceberg dynamics, as well as interactions within biogeochemical cycles. Specifically, we used temperature tendency heat budgets available in MOM4p1⁵⁰ (<https://github.com/mom-ocean/MOM4p1>). This ocean model uses a tripolar horizontal grid of 1° x 1°, increasing meridionally to up to 1/3° towards the Equator, and with 50 depth levels. We analysed daily-mean outputs of all tendency terms that change the SST (over the upper 10 m) from a 500-yr preindustrial control simulation (with atmospheric CO₂, along with all other agents that influence radiation fixed at their preindustrial levels) and confirmed with an eight-member ensemble simulation of the GFDL ESM2M driven by historical data and the Representative Concentration Pathway 8.5 (RCP8.5) scenario from 1982 to 2021, following refs. 51,86.

For each grid cell, the model dissects the total heat change (ΔQ_{total}) across time intervals into various heat budget components. These components signify temperature changes due to distinct processes modelled. The total tendency of heat at the ocean surface, in W m⁻², is determined by Eq. (4)⁵⁰:

$$\Delta Q_{\text{total}} = \Delta Q_{\text{adv}} + \Delta Q_{\text{a-s}} + \Delta Q_{\text{vmix}} + \Delta Q_{\text{vdiff}} + \Delta Q_{\text{res}} \quad (4)$$

where ΔQ_{adv} represent the change in heat resulting from both horizontal and vertical advective heat fluxes, both explicitly resolved and approximated on subgrid scales through parameterisation. $\Delta Q_{\text{a-s}}$ is the air-sea exchange of heat, including the balance of shortwave radiation (the net incoming surface shortwave radiation reduced by the fraction of shortwave radiation that goes beyond the surface layer) along with the net incoming longwave radiation, in addition to the net fluxes of latent and sensible heat⁸⁵. ΔQ_{vmix} refers to the heat flux generated by the non-local segment of the K-profile parameterization (KPP)⁵⁰, representing convective vertical mixing within the ocean boundary layer in response to negative buoyancy forcing. ΔQ_{vdiff} accounts for heat fluxes caused by vertical diffusion, encompassing vertical mixing within the ocean boundary layer attributed to the local component of the KPP, as well as tidal mixing. Furthermore, the residual term (ΔQ_{res}) includes other smaller processes such as heat exchange due to river runoff, solid runoff from iceberg calving, neutral diffusion, or the heat flux exchange resulting from interactions of surface water masses due to precipitation and evaporation. A detailed description of each term can be found in Supplementary Methods S1, Supplementary equations(S1–6), and also in ref. 50.

We then computed anomalies of all these heat budget terms relative to their seasonal cycles for each ocean grid cell, to ultimately average them separately over the days of the onset (build-up of heat) and decay (dissipation of heat) phases of the MHWs (see Supplementary Fig. S1). Moreover, based on the change in heat content, the change in potential temperature ($\Delta\theta$), in °C d⁻¹, can be approximated using Eq. (5)⁵⁰:

$$\Delta\theta = \frac{\Delta Q_{\text{total}}}{C_p^0 \rho_0 dz}, \quad (5)$$

where C_p^0 is a fixed value for heat capacity, set at 3992.1 J kg⁻¹K⁻¹ in MOM4p1; ρ_0 is the constant Boussinesq density of 1.035 kg m⁻³, and dz is the changing thickness of vertical grid cells over time, measured in m, as described by ref. 50. In our analysis, we assumed a thickness of $dz = 10$ m, which led to a conversion factor of 0.00209 °C m² s⁻¹ W⁻¹. This inference is justified because the real fluctuations in the thickness of grid cells differ minimally (with the largest changes being around 1·10⁻² in the open ocean), resulting in negligible adjustments to the conversion factor. Despite the fact that these errors can accumulate over time, for time scales of MHW durations (days to few months), they are significantly reduced, as demonstrated by ref. 51.

The motivation for using the GFDL ESM2M (MOM4p1) model for the assessment of local physical drivers of MHWs in the Southern Ocean was due to the good agreement between the climatological characteristics and the trends of modelled and observation-based MHWs globally^{26,51,86}, as a result of the model's fidelity in simulating the mean state and interannual

variations in SST. Moreover, in the SO outside the sea ice area, the model fits well with observational data^{26,51}.

Approaches to trend analysis

Trends in MHW properties are usually explained by changes in either mean or trend in higher-order SST statistics. Anthropogenic climate change-associated mean warming SST is considered to be the main driver of the increasing MHW frequency over 2/3 of the global ocean^{20,69}. In this study, we also characterised trends and variability in MHW properties south of 40°S using an ordinary least squares estimator of linear trend. Therefore, in order to avoid biases due to non-normally distributed data we used Theil-Sen (TS)⁸⁷ estimates to obtain linear trends of the circumpolarly averaged time series. The code followed to compute these trends and generate the results can be freely obtained from https://github.com/ecjoliver/Global_MHW_Trends. The statistical significance of MHW trends was carried out using a 95% confidence level.

To better analyse trends in nutrients (Fe, NO₃, Si, PO₄) and CHL concentrations, as well as in primary production rates and its statistical significance, a modified non-parametric Mann-Kendall test⁸⁸ was applied, which is a variance correction method for taking into account the serial autocorrelation, differing from the original Mann-Kendall test⁸⁹ and requires serially-independent data, not considering seasonal effects. The xarrayMannKendall Python module implemented by ref. 90. (<https://github.com/josuertzmo/xarrayMannKendall>) was subsequently computed adjusting the effective number of degrees of freedom for autocorrelation ($\alpha = 0.05$).

Causal interactions through empirical dynamic modelling

In an effort to investigate the causal interactions among the key variables in our study (Max. SSTA, NPP, SIC, and MLD), we applied Empirical Dynamic Modelling (EDM). This cutting-edge framework is based on Takens' theorem, which provides tools for attractor reconstruction⁹¹ and allows for the modelling of causal relationships in nonlinear dynamic systems in the absence of governing dynamic equations⁶⁵. In dynamical systems, two state variables X and Y are considered to be causally linked if they contain shared information that allows reconstruction of the observed dynamics from one state variable, say X, from the dynamics of the other variable, Y. This shared information can allow for a unidirectional reconstruction (e.g., X causes Y), or a bidirectional reconstruction (both variables cause each other) of the dynamics⁶⁵. In essence, Takens' theorem shows that the dynamics of a state variable Y caused by another variable X is encoded in the delayed-coordinates embedding⁶⁵ of the causing variable, X in this case. This is provided by the so-called attractor manifold M which, in the absence of a governing dynamics equation, contains all the information needed to encode the dynamic system: it is the region of the state space that contains all the possible states of the system in the long-term. The essential assumption of EDM is that causality within a dynamic system is more strongly dependent on the proximity of the values of the variables in the state space than in their proximity in time^{65,91}. In our analysis, we applied Convergent Cross Mapping (CCM), introduced by ref. 65 to perform the nonlinear state space reconstruction. CCM assesses causality by evaluating how accurately the historical data of Y can predict the state of X, or viceversa. This prediction is feasible only if Y has a causal impact on X. To delve deeper, CCM seeks evidence of X's influence within Y's time series by examining if the 'library' of points (L) in the attractor constructed from Y, denoted as M_Y , matches with the points in X's attractor, M_X . Both manifolds, M_Y and M_X , are formed from the time-delayed coordinates of the variables Y and X, respectively⁶⁵.

Considering two time series of length l , $\{X\} = \{X(1), X(2), \dots, X(l)\}$ and $\{Y\} = \{Y(1), Y(2), \dots, Y(l)\}$, we created delay embedding vectors from a time series following Eq. (6):

$$\begin{aligned} x(t) &= [X(t), X(t - \tau), X(t - 2\tau), \dots, X(t - (E - 1)\tau)] \\ \text{for } t &= 1 + (E - 1)\tau \text{ to } t = l \end{aligned} \quad (6)$$

where τ is the time delay (i.e., lag), E is the embedding dimension, and t is time. These vectors form the 'reconstructed manifold' or 'shadow manifold' (M_X). To create a cross-mapped prediction of $Y(t)$, expressed as $\hat{Y}(t)|M_X$, we started by locating the corresponding lagged-coordinate vector on M_X , $x(t)$, and then identifying its $E + 1$ nearest neighbors. We then labelled the time indices of these $E + 1$ nearest neighbours of $x(t)$, in order from nearest to furthest, as t_1, \dots, t_{E+1} (Eq. (7)). These specific time indices, which were closest to $x(t)$ on M_X , were used to locate corresponding points (neighbours) in Y (considered a prospective neighbourhood) to approximate $Y(t)$ through a locally weighted average of the $E + 1$ values of $Y(t_i)$.

$$\hat{Y}(t)|M_X = \sum w_i Y(t_i), i = 1 \dots E + 1; \quad (7)$$

where w_i is a weighting that is determined by the Euclidean distance between $x(t)$ and its i^{th} closest neighbour within M_X and $Y(t_i)$ are the concurrent values of Y . The strength of this cross-mapping and its convergence as the l increases serve as evidence of causality⁶⁵.

We applied CCM on monthly time series of Max. SSTA, NPP, SIC, and MLD from 1998 to 2021 (288 values) corresponding to each ocean grid cell. Although CCM is regarded as a non-parametric method, the selection of the τ and E parameters must indeed be conducted with care to ensure that the phase space reconstruction accurately reflects the true dynamics of the system. Therefore, in our analysis, we performed a sensitivity test via mutual information to identify the τ value that maximises the shared information between $X(t)$ and $X(t - \tau)$, thereby indicating the most effective delay, following ref. 92. Furthermore, we also determined the minimum embedding dimension required for the reconstructed phase space to unfold the system's dynamics (Supplementary Fig. S10). From this, we obtained an optimal τ of 3 (which is coherent with seasonal time scales) and an $E = 6$. To quantify the prediction skill, CCM uses the Pearson's correlation coefficient between the actual states of the system (e.g., the true values of Y) and the predicted states (using the reconstructed dynamics from X). High correlation suggested a strong causal link, where the ability to predict Y from X suggested that X has a causal influence on Y .

Given their minimal assumptions, EDM and concretely CCM, is especially robust for analysing systems that exhibit strongly non-equilibrium dynamics and nonlinear behaviour, where interactions vary over time and depend on the system's current state⁶⁵. That is to say, these approaches are particularly suitable for studying NPP dynamics under a changing SO.

Data availability

All datasets used in this study are publicly available online. New data were not generated as a result of this study. ESA CCI & C3S SST, SIC reanalysis data, GLORYS12V1 MLD, and the global ocean biogeochemical L4 products are freely available at CMS: <https://data.marine.copernicus.eu/products> (last access: March 2024). The ECMWF ERA5 N-SAT can be found at: <https://www.ecmwf.int/en/forecasts/dataset/ecmwf-reanalysis-v5> (last access: November 2023). The CbPM NPP product can be retrieved from http://orca.science.oregonstate.edu/npp_products.php (last access: November 2023). The climate indices as metrics for climate modes used in this study are freely available at: <https://psl.noaa.gov/data/climateindices/list/> (ONI and TSA; last access: November 2023), while the observation-based SAM Index can be obtained from www.antarctica.ac.uk/met/gjma/sam.html (last access: November 2023). All these URL addresses are also listed in the Methods section. All outputs from the analysis of heat budget in MOM4p1 (ESM2M GFDL) and also causal inference through CCM between physical variables and NPP rates are freely accessible at <https://doi.org/10.20350/digitalCSIC/16360>⁹³.

Code availability

All the codes developed to carry out this study are available upon request via GitHub: <https://github.com/ManuFBarba/Southern-Ocean-MHWs.git>.

MHW analysis was performed following the codes developed by E.C.J. Oliver: <https://github.com/ecjoliver/marineHeatWaves> and https://github.com/ecjoliver/Global_MHW_Trends. We also applied the xarray-MannKendall Python module (<https://github.com/josuemtzmo/xarrayMannKendall>). The quick-start guide for running the GFDL ESM2M codes is publicly available in <https://mom-ocean.github.io/docs/quick-start-guide/> and can also be accessed through <https://github.com/moment/MOM4p1>. The EDM (CCM) analysis was conducted using the Python module (pyEDM) developed by Sugihara, as documented at: <https://github.com/SugiharaLab/pyEDM> and https://sugiharalab.github.io/EDM_Documentation/ccm/. Matplotlib and Cartopy (<https://matplotlib.org/>, <https://scitools.org.uk/cartopy/docs/latest/>) modules from Python 3.10.11 were used for plotting. The coastlines on the maps are derived from the Global Self-consistent, Hierarchical, High-resolution Geography datasets (GSHHG) (www.soest.hawaii.edu/pwessel/gshhg/), which has been distributed under the GNU Lesser General Public License and provided with the Python Cartopy module.

Received: 30 November 2023; Accepted: 8 July 2024;

Published online: 27 July 2024

References

- Masson-Delmotte, V., et al. M. Huang, K. Leitzell, E. Lonnoy, J. B. R. Matthews, T. K. Maycock, T. Waterfield, O. Yelekçi, R. Yu & B. Zhou (eds.). IPCC. Climate Change 2021: The Physical Science Basis. Contribution of Working Group I to the Sixth Assessment Report of the Intergovernmental Panel on Climate Change.
- Wunderling, N. et al. Global warming overshoots increase risks of climate tipping cascades in a network model. *Nat. Clim. Chang.* **13**, 75–82 (2023).
- Oliver, E. C. J. et al. Longer and more frequent marine heatwaves over the past century. *Nat. Commun.* **9**, 1324 (2018).
- Oliver, E. C. J. et al. Projected Marine Heatwaves in the 21st Century and the Potential for Ecological Impact. *Front. Mar. Sci.* **6**, 734 (2019).
- Frölicher, T. L. & Laufkötter, C. Emerging risks from marine heatwaves. *Nat. Commun.* **9**, 650 (2018).
- Smale, D. A. et al. Marine heatwaves threaten global biodiversity and the provision of ecosystem services. *Nat. Clim. Chang.* **9**, 306–312 (2019).
- Gomes, D. G. E. et al. Marine heatwaves disrupt ecosystem structure and function via altered food webs and energy flux. *Nat. Commun.* **15**, 1988 (2024).
- Hobday, A. J. et al. A hierarchical approach to defining marine heatwaves. *Prog. Oceanogr.* **141**, 227–238 (2016).
- Hobday, A. et al. Categorizing and Naming Marine Heatwaves. *Oceanography* **31**, 162–173 (2018).
- Holbrook, N. J. et al. Keeping pace with marine heatwaves. *Nat. Rev. Earth Environ.* **1**, 482–493 (2020).
- Burrows, M. T. et al. Ocean community warming responses explained by thermal affinities and temperature gradients. *Nat. Clim. Chang.* **9**, 959–963 (2019).
- Stuart-Smith, R. D., Edgar, G. J., Barrett, N. S., Kininmonth, S. J. & Bates, A. E. Thermal biases and vulnerability to warming in the world's marine fauna. *Nature* **528**, 88–92 (2015).
- Andrew, S. M., Morell, H. T., Strzepek, R. F., Boyd, P. W. & Ellwood, M. J. Iron Availability Influences the Tolerance of Southern Ocean Phytoplankton to Warming and Elevated Irradiance. *Front. Mar. Sci.* **6**, 681 (2019).
- Smith, K. E. et al. Biological Impacts of Marine Heatwaves. *Annu. Rev. Mar. Sci.* **15**, 119–145 (2023).
- Caputi, N. et al. Management adaptation of invertebrate fisheries to an extreme marine heat wave event at a global warming hot spot. *Ecol. Evol.* **6**, 3583–3593 (2016).
- Cheung, W. W. L. & Frölicher, T. L. Marine heatwaves exacerbate climate change impacts for fisheries in the northeast Pacific. *Sci. Rep.* **10**, 6678 (2020).
- Wyatt, A. M., Resplandy, L. & Marchetti, A. Ecosystem impacts of marine heat waves in the northeast Pacific. *Biogeosciences* **19**, 5689–5705 (2022).
- Hughes, T. P. et al. Global warming and recurrent mass bleaching of corals. *Nature* **543**, 373–377 (2017).
- Garrabou, J. et al. Marine heatwaves drive recurrent mass mortalities in the Mediterranean Sea. *Glob. Change Biol.* **28**, 5708–5725 (2022).
- Oliver, E. C. J. et al. Marine Heatwaves. *Annu. Rev. Mar. Sci.* **13**, 313–342 (2021).
- Xu, T. et al. An increase in marine heatwaves without significant changes in surface ocean temperature variability. *Nat. Commun.* **13**, 7396 (2022).
- Sen Gupta, A. et al. Drivers and impacts of the most extreme marine heatwave events. *Sci. Rep.* **10**, 19359 (2020).
- Holbrook, N. J. et al. A global assessment of marine heatwaves and their drivers. *Nat. Commun.* **10**, 2624 (2019).
- Thoral, F. et al. Unravelling seasonal trends in coastal marine heatwave metrics across global biogeographical realms. *Sci. Rep.* **12**, 7740 (2022).
- Jacox, M. G. et al. Global seasonal forecasts of marine heatwaves. *Nature* **604**, 486–490 (2022).
- Frölicher, T. L., Fischer, E. M. & Gruber, N. Marine heatwaves under global warming. *Nature* **560**, 360–364 (2018).
- Huang, B. et al. Prolonged Marine Heatwaves in the Arctic: 1982–2020. *Geophys. Res. Lett.* **48**, e2021GL095590 (2021).
- Wille, J. D. et al. Antarctic Atmospheric River Climatology and Precipitation Impacts. *JGR Atmos.* **126**, e2020JD033788 (2021).
- Ludescher, J., Yuan, N. & Bunde, A. Detecting the statistical significance of the trends in the Antarctic sea ice extent: an indication for a turning point. *Clim. Dyn.* **53**, 237–244 (2019).
- Adusumilli, S., Fricker, H. A., Medley, B., Padman, L. & Siegfried, M. R. Interannual variations in meltwater input to the Southern Ocean from Antarctic ice shelves. *Nat. Geosci.* **13**, 616–620 (2020).
- Wang, G. et al. Future Southern Ocean warming linked to projected ENSO variability. *Nat. Clim. Chang.* **12**, 649–654 (2022).
- Li, J., Roughan, M. & Kerr, C. Drivers of ocean warming in the western boundary currents of the Southern Hemisphere. *Nat. Clim. Chang.* **12**, 901–909 (2022).
- Swart, N. C., Gille, S. T., Fyfe, J. C. & Gillett, N. P. Recent Southern Ocean warming and freshening driven by greenhouse gas emissions and ozone depletion. *Nat. Geosci.* **11**, 836–841 (2018).
- Bronsemaer, B. et al. Importance of wind and meltwater for observed chemical and physical changes in the Southern Ocean. *Nat. Geosci.* **13**, 35–42 (2020).
- Shi, J.-R., Talley, L. D., Xie, S.-P., Peng, Q. & Liu, W. Ocean warming and accelerating Southern Ocean zonal flow. *Nat. Clim. Chang.* **11**, 1090–1097 (2021).
- Arblaster, J. M. & Meehl, G. A. Contributions of External Forcings to Southern Annular Mode Trends. *J. Clim.* **19**, 2896–2905 (2006).
- Liu, W. et al. Stratospheric ozone depletion and tropospheric ozone increases drive Southern Ocean interior warming. *Nat. Clim. Chang.* **12**, 365–372 (2022).
- Oh, J.-H. et al. Antarctic meltwater-induced dynamical changes in phytoplankton in the Southern Ocean. *Environ. Res. Lett.* **17**, 024022 (2022).
- Thomalla, S. J., Nicholson, S.-A., Ryan-Keogh, T. J. & Smith, M. E. Widespread changes in Southern Ocean phytoplankton blooms linked to climate drivers. *Nat. Clim. Chang.* **13**, 975–984 (2023).
- Noh, K. M., Lim, H.-G. & Kug, J.-S. Global chlorophyll responses to marine heatwaves in satellite ocean color. *Environ. Res. Lett.* **17**, 064034 (2022).

41. Hayashida, H., Matear, R. J. & Strutton, P. G. Background nutrient concentration determines phytoplankton bloom response to marine heatwaves. *Glob. Change Biol.* **26**, 4800–4811 (2020).
42. Wang, Y.-L., Hsu, Y.-C., Lee, C.-P. & Wu, C.-R. Coupling Influences of ENSO and PDO on the Inter-Decadal SST Variability of the ACC around the Western South Atlantic. *Sustainability* **11**, 4853 (2019).
43. Banzon, V., Smith, T. M., Steele, M., Huang, B. & Zhang, H.-M. Improved Estimation of Proxy Sea Surface Temperature in the Arctic. *J. Atmos. Ocean. Technol.* **37**, 341–349 (2020).
44. Blanchard-Wrigglesworth, E., Roach, L. A., Donohoe, A. & Ding, Q. Impact of Winds and Southern Ocean SSTs on Antarctic Sea Ice Trends and Variability. *J. Clim.* **34**, 949–965 (2021).
45. Carvalho, K. S., Smith, T. E. & Wang, S. Bering Sea marine heatwaves: Patterns, trends and connections with the Arctic. *J. Hydrol.* **600**, 126462 (2021).
46. Marin, M., Feng, M., Phillips, H. E. & Bindoff, N. L. A. Global, Multiproduct Analysis of Coastal Marine Heatwaves: Distribution, Characteristics, and Long-Term Trends. *J. Geophys. Res. Oceans* **126**, e2020JC016708 (2021).
47. Li, X. et al. Tropical teleconnection impacts on Antarctic climate changes. *Nat. Rev. Earth Environ.* **2**, 680–698 (2021).
48. Noh, K. M., Lim, H.-G. & Kug, J.-S. Zonally asymmetric phytoplankton response to the Southern annular mode in the marginal sea of the Southern ocean. *Sci. Rep.* **11**, 10266 (2021).
49. Yook, S., Thompson, D. W. J. & Solomon, S. Climate Impacts and Potential Drivers of the Unprecedented Antarctic Ozone Holes of 2020 and 2021. *Geophys. Research Lett.* **49**, e2022GL098064 (2022).
50. Griffies, S. M. Working notes on the ocean heat budget in GFDL-ESM2M. https://mom-ocean.github.io/assets/pdfs/ESM2M_heat_budget.pdf [Accessed February 8, 2024]. (2015).
51. Vogt, L., Burger, F. A., Griffies, S. M. & Frölicher, T. L. Local Drivers of Marine Heatwaves: A Global Analysis With an Earth System Model. *Front. Clim.* **4**, 847995 (2022).
52. Stuecker, M. F., Bitz, C. M. & Armour, K. C. Conditions leading to the unprecedented low Antarctic sea ice extent during the 2016 austral spring season: RECORD LOW 2016 ANTARCTIC SEA ICE EXTENT. *Geophys. Res. Lett.* **44**, 9008–9019 (2017).
53. Holland, M. M., Landrum, L., Raphael, M. N. & Kwok, R. The Regional, Seasonal, and Lagged Influence of the Amundsen Sea Low on Antarctic Sea Ice. *Geophys. Res. Lett.* **45**, 11–227 (2018).
54. Wang, Z., Turner, J., Wu, Y. & Liu, C. Rapid Decline of Total Antarctic Sea Ice Extent during 2014–16 Controlled by Wind-Driven Sea Ice Drift. *J. Clim.* **32**, 5381–5395 (2019).
55. Kwok, R., Pang, S. S. & Kacimi, S. Sea ice drift in the Southern Ocean: Regional patterns, variability, and trends. *Elementa: Sci. Anthropocene* **5**, 32 (2017).
56. Turner, J. et al. Atmosphere-ocean-ice interactions in the Amundsen Sea Embayment, West Antarctica: The Amundsen Sea Embayment, Antarctica. *Rev. Geophys.* **55**, 235–276 (2017).
57. Meehl, G. A., Arblaster, J. M., Bitz, C. M., Chung, C. T. Y. & Teng, H. Antarctic sea-ice expansion between 2000 and 2014 driven by tropical Pacific decadal climate variability. *Nat. Geosci.* **9**, 590–595 (2016).
58. Schlosser, E., Haumann, F. A. & Raphael, M. N. Atmospheric influences on the anomalous 2016 Antarctic sea ice decay. *Cryosphere* **12**, 1103–1119 (2018).
59. Pinkerton, M. H. et al. Evidence for the Impact of Climate Change on Primary Producers in the Southern Ocean. *Front. Ecol. Evol.* **9**, 592027 (2021).
60. Lannuzel, D. et al. Iron in sea ice: Review and new insights. *Elementa: Sci. Anthropocene* **4**, 000130 (2016).
61. Moreau, S., Boyd, P. W. & Strutton, P. G. Remote assessment of the fate of phytoplankton in the Southern Ocean sea-ice zone. *Nat. Commun.* **11**, 3108 (2020).
62. Uchida, T. et al. Vertical eddy iron fluxes support primary production in the open Southern Ocean. *Nat. Commun.* **11**, 1125 (2020).
63. Boyd, P. W. et al. The role of biota in the Southern Ocean carbon cycle. *Nat. Rev. Earth Environ.* <https://doi.org/10.1038/s43017-024-00531-3> (2024).
64. Cabanes, D. J. E. et al. Using Fe chemistry to predict Fe uptake rates for natural plankton assemblages from the Southern Ocean. *Mar. Chem.* **225**, 103853 (2020).
65. Sugihara, G. et al. Detecting Causality in Complex Ecosystems. *Science* **338**, 496–500 (2012).
66. Meehl, G. A. et al. Sustained ocean changes contributed to sudden Antarctic sea ice retreat in late 2016. *Nat. Commun.* **10**, 14 (2019).
67. Deppeler, S. L. & Davidson, A. T. Southern Ocean Phytoplankton in a Changing Climate. *Front. Mar. Sci.* **4**, 40 (2017).
68. Montes-Hugo, M. et al. Recent Changes in Phytoplankton Communities Associated with Rapid Regional Climate Change Along the Western Antarctic Peninsula. *Science* **323**, 1470–1473 (2009).
69. Oliver, E. C. J. Mean warming not variability drives marine heatwave trends. *Clim. Dyn.* **53**, 1653–1659 (2019).
70. Montie, S., Thomsen, M. S., Rack, W. & Broady, P. A. Extreme summer marine heatwaves increase chlorophyll *a* in the Southern Ocean. *Antarct. Sci.* **32**, 508–509 (2020).
71. Fragkoupolou, E. et al. Marine biodiversity exposed to prolonged and intense subsurface heatwaves. *Nat. Clim. Chang.* **13**, 1114–1121 (2023).
72. Belyaev, O. et al. The contribution of penguin guano to the Southern Ocean iron pool. *Nat. Commun.* **14**, 1781 (2023).
73. Ibarbalz, F. M. et al. Global Trends in Marine Plankton Diversity across Kingdoms of Life. *Cell* **179**, 1084–1097.e21 (2019).
74. Merchant, C. J. et al. Sea surface temperature datasets for climate applications from Phase 1 of the European Space Agency Climate Change Initiative (sst cci). *Geosci. Data J.* **1**, 179–191 (2014).
75. Merchant, C. J. et al. Satellite-based time-series of sea-surface temperature since 1981 for climate applications. *Sci. Data* **6**, 223 (2019).
76. Hersbach, H. et al. The ERA5 global reanalysis. *Q. J. R. Meteorol. Soc.* **146**, 1999–2049 (2020).
77. Gossart, A. et al. An Evaluation of Surface Climatology in State-of-the-Art Reanalyses over the Antarctic Ice Sheet. *J. Clim.* **32**, 6899–6915 (2019).
78. Tetzner, D., Thomas, E. & Allen, C. A Validation of ERA5 Reanalysis Data in the Southern Antarctic Peninsula—Ellsworth Land Region, and Its Implications for Ice Core Studies. *Geosciences* **9**, 289 (2019).
79. Zhu, J. et al. An Assessment of ERA5 Reanalysis for Antarctic Near-Surface Air Temperature. *Atmosphere* **12**, 217 (2021).
80. Westberry, T., Behrenfeld, M. J., Siegel, D. A. & Boss, E. Carbon-based primary productivity modeling with vertically resolved photoacclimation. *Global Biogeochem. Cycles* **22**, <https://doi.org/10.1029/2007GB003078> (2008).
81. Behrenfeld, M. J., Boss, E., Siegel, D. A. & Shea, D. M. Carbon-based ocean productivity and phytoplankton physiology from space. *Global Biogeochem. Cycles* **19**, <https://doi.org/10.1029/2004GB002299> (2005).
82. Le Grix, N., Zscheischler, J., Rodgers, K. B., Yamaguchi, R. & Frölicher, T. L. Hotspots and drivers of compound marine heatwaves and low net primary production extremes. *Biogeosciences* **19**, 5807–5835 (2022).
83. Maynard, J. A. et al. *ReefTemp*: An interactive monitoring system for coral bleaching using high-resolution SST and improved stress predictors. *Geophys. Res. Lett.* **35**, L05603 (2008).
84. Enfield, D. B., Mestas-Nuñez, A. M., Mayer, D. A. & Cid-Serrano, L. How ubiquitous is the dipole relationship in tropical Atlantic sea surface temperatures? *J. Geophys. Res.* **104**, 7841–7848 (1999).
85. Dunne, J. P. et al. GFDL's ESM2 Global Coupled Climate–Carbon Earth System Models. Part II: Carbon System Formulation and Baseline Simulation Characteristics*. *J. Clim.* **26**, 2247–2267 (2013).

86. Burger, F. A., Terhaar, J. & Frölicher, T. L. Compound marine heatwaves and ocean acidity extremes. *Nat. Commun.* **13**, 4722 (2022).
87. Sen, P. K. Estimates of the Regression Coefficient Based on Kendall's Tau. *J. Am. Stat. Assoc.* **63**, 1379–1389 (1968).
88. Yue, S. & Wang, C. The Mann-Kendall Test Modified by Effective Sample Size to Detect Trend in Serially Correlated Hydrological Series. *Water Resour. Manag.* **18**, 201–218 (2004).
89. Kendall, M. G. *Rank Correlation Measures*; Charles Griffin Book Series. (1975).
90. Moreno, J. M. & Constantinou, N. C. *josuemtzmo/xarrayMannKendall*: Mann Kendall significance test implemented in xarray. Zenodo <https://doi.org/10.5281/ZENODO.4458777> (2021).
91. Takens, F. Detecting strange attractors in turbulence. In *Dynamical Systems and Turbulence, Warwick 1980* (eds. Rand, D. & Young, L.-S.) vol. 898 366–381 (Springer Berlin Heidelberg, Berlin, Heidelberg, 1981).
92. Ye, H., Deyle, E. R., Gilarranz, L. J. & Sugihara, G. Distinguishing time-delayed causal interactions using convergent cross mapping. *Sci. Rep.* **5**, 14750 (2015).
93. Fernández-Barba, M., Belyaev, O., Huertas, I. E. & Navarro, G. Marine Heatwaves in a Changing Southern Ocean: Heat Budget Analysis in Modular Ocean Model v4p1 (ESM2M GFDL) and Causal Inference through Convergent Cross Mapping. DIGITAL.CSIC <https://doi.org/10.20350/DIGITALCSIC/16360> (2024).
94. Chapman, C. C., Lea, M.-A., Meyer, A., Sallée, J.-B. & Hindell, M. Defining Southern Ocean fronts and their influence on biological and physical processes in a changing climate. *Nat. Clim. Chang.* **10**, 209–219 (2020).

Acknowledgements

This research has been financially supported by the Spanish grants DICHOSO (PID2021–125783OBI00) and PIMETAN (ref. RTI2018-098048-B-I00) funded by MCIN/AEI/10.13039/501100011033 and by “ERDF A way of making Europe”. M.F.B. is supported by the European Social Fund and the Youth Employment Initiative through the “Programa Operativo Fondo Social Europeo. Contratación Jóvenes Investigadores I + D + I”. The authors thank all members of Copernicus Marine and Atmosphere Monitoring Services and of the NOAA Geophysical Fluid Dynamics Laboratory for their technical support. We also appreciate assistance from M. B. Dunbar and S. Heredia Carmona, both from the Institute of Marine Sciences of Andalusia, Spanish National Research Council (ICMAN-CSIC) for the English language revision and technical assistance with programming, respectively. Furthermore, we thank P. Almaraz, from the ICMAN-CSIC, for his staunch support with the implementation and interpretation of EDM. This research is a contribution to the CSIC Interdisciplinary Thematic Platforms PTI-POLARCSIC, PTI-TELEDETECT and PTI-Oceans + .

Author contributions

M.F.B. performed the analysis and wrote the first draft of the manuscript under I.E.H. and G.N.'s supervision. O.B. edited the figures. M.F.B., I.E.H. and G.N. led the research proposing central ideas. All the authors contributed equally to discussing the results and approving the submitted version of the manuscript.

Competing interests

The authors declare no competing interests.

Additional information

Supplementary information The online version contains supplementary material available at <https://doi.org/10.1038/s43247-024-01553-x>.

Correspondence and requests for materials should be addressed to Manuel Fernández-Barba.

Peer review information *Communications Earth & Environment* thanks Lei Zhang, Christopher Chapman and the other, anonymous, reviewer(s) for their contribution to the peer review of this work. Primary Handling Editors: Weiqing Han, Joe Aslin, Clare Davis, Heike Langenberg. A peer review file is available.

Reprints and permissions information is available at <http://www.nature.com/reprints>

Publisher's note Springer Nature remains neutral with regard to jurisdictional claims in published maps and institutional affiliations.

Open Access This article is licensed under a Creative Commons Attribution-NonCommercial-NoDerivatives 4.0 International License, which permits any non-commercial use, sharing, distribution and reproduction in any medium or format, as long as you give appropriate credit to the original author(s) and the source, provide a link to the Creative Commons licence, and indicate if you modified the licensed material. You do not have permission under this licence to share adapted material derived from this article or parts of it. The images or other third party material in this article are included in the article's Creative Commons licence, unless indicated otherwise in a credit line to the material. If material is not included in the article's Creative Commons licence and your intended use is not permitted by statutory regulation or exceeds the permitted use, you will need to obtain permission directly from the copyright holder. To view a copy of this licence, visit <http://creativecommons.org/licenses/by-nc-nd/4.0/>.

© The Author(s) 2024